The Astrophysical Journal, 806:214 (11pp), 2015 June 20 doi:10.1088/0004-637X/806/2/214

LABORATORY MEASUREMENTS OF WHITE DWARF PHOTOSPHERIC SPECTRAL LINES: Hβ

Ross E. Falcon[1,2], G. A. Rochau[2], J. E. Bailey[2], T. A. Gomez[1,2], M. H. Montgomery[1], D. E. Winget[1], and T. Nagayama[2]
[1] Department of Astronomy and McDonald Observatory, University of Texas, Austin, TX, 78712; mikemon@astro.as.utexas.edu, dew@astro.as.utexas.edu
[2] Sandia National Laboratories, Albuquerque, NM 87185-1196, USA; refalco@sandia.gov, garocha@sandia.gov, jebaile@sandia.gov, gomezt@astro.as.utexas.edu, tnnagay@sandia.gov
Received 2015 February 10; accepted 2015 May 14; published 2015 June 18

ABSTRACT

We spectroscopically measure multiple hydrogen Balmer line profiles from laboratory plasmas to investigate the theoretical line profiles used in white dwarf (WD) atmosphere models. X-ray radiation produced at the *Z* Pulsed Power Facility at Sandia National Laboratories initiates plasma formation in a hydrogen-filled gas cell, replicating WD photospheric conditions. Here we present time-resolved measurements of Hβ and fit this line using different theoretical line profiles to diagnose electron density, n_e, and $n = 2$ level population, n_2. Aided by synthetic tests, we characterize the validity of our diagnostic method for this experimental platform. During a single experiment, we infer a continuous range of electron densities increasing from $n_e \sim 4$ to $\sim 30 \times 10^{16}$ cm^{-3} throughout a 120-ns evolution of our plasma. Also, we observe n_2 to be initially elevated with respect to local thermodynamic equilibrium (LTE); it then equilibrates within ~55 ns to become consistent with LTE. This supports our electron-temperature determination of $T_e \sim 1.3$ eV (~15,000 K) after this time. At $n_e \gtrsim 10^{17}$ cm^{-3}, we find that computer-simulation-based line-profile calculations provide better fits (lower reduced χ^2) than the line profiles currently used in the WD astronomy community. The inferred conditions, however, are in good quantitative agreement. This work establishes an experimental foundation for the future investigation of relative shapes and strengths between different hydrogen Balmer lines.

Key words: line: profiles – methods: laboratory: atomic – plasmas – techniques: spectroscopic – white dwarfs

1. INTRODUCTION

Recently, Tremblay & Bergeron (2009, hereafter TB) revamped white dwarf (WD) atmosphere models by modifying the constituent theoretical hydrogen line profiles, which are calculated using the Unified Theory of Stark broadening (Smith et al. 1969; Vidal et al. 1970, 1971, 1973, hereafter VCS). They followed the lead of Seaton (1990) to incorporate the occupation probability formalism of Hummer & Mihalas (1988) into the line-profile calculation to account for the loss of upper-energy-level transitions due to the high electric microfields common in WD-atmosphere plasmas. This significantly improves the consistency of effective temperature, $T_{\rm eff}$, and surface gravity, $\log g$, inferred from different, spectroscopically observed hydrogen Balmer lines. It also results in a systematic increase in both $T_{\rm eff}$ and $\log g$.

TB used their line profiles to spectroscopically determine an increased mean mass of $\langle M \rangle = 0.649\,M_\odot$ for DA WDs from the Palomar–Green Survey (Liebert et al. 2005). Falcon et al. (2010a) used gravitational redshifts—a method mostly independent of theoretical line profiles—to infer a DA mean mass of $\langle M \rangle = 0.647^{+0.013}_{-0.014}\,M_\odot$ from the European Southern Observatory SNe Ia progenitor survey (Napiwotzki et al. 2001). This is in excellent agreement with TB. Subsequent spectroscopic studies using TB line profiles, however, do not find mean masses from other WD samples that agree with that determined from Falcon et al. (2010a). These include Limoges & Bergeron (2010), Tremblay et al. (2011), and Kleinman et al. (2013), who found $\langle M \rangle = 0.606$, 0.613, and $0.623\,M_\odot$, respectively.

The impact of theoretical line profiles on the interpretation of observed WD spectra as well as the discrepancy between the inferred mean masses from the spectroscopic and gravitational-redshift methods motivate the development of laboratory experiments capable of testing line-profile theories. TB profiles now replace the tabulated VCS profiles of Lemke (1997) as the WD-astronomy standard. The difference between these calculations increases with increasing principal quantum number, n, and with electron density, n_e. Therefore, measurements of the *relative* line *shapes* of hydrogen Balmer lines formed at high electron densities can be used to discriminate between theoretical line-profile models. However, few laboratory experiments push into high n_e ($\gtrsim 10^{17}$ cm^{-3}) for the investigation of H line shapes (e.g., Morris & Krey 1968; Parigger et al. 2003, 2008; Djurović et al. 2005, 2009), and none of these measure multiple lines in the same plasma. Simultaneous measurements of multiple lines is highly desirable because it alleviates potential systematic uncertainties and promotes measurement accuracy.

Our experiments create plasmas at WD photospheric conditions and reach $n_e > 10^{17}$ cm^{-3} while simultaneously observing multiple spectral lines (Falcon et al. 2010b, 2013a, 2013b; Montgomery et al. 2015). Hence, we provide the first such laboratory data at these plasma conditions; we do so using a fundamentally different experimental approach than previous studies (e.g., Wiese et al. 1963; Hill & Gerardo 1967; Bengtson et al. 1969; Helbig & Nick 1981) by radiatively driving plasma formation (e.g., Mancini et al. 2009; Liedahl 2011). Because we use time-resolved spectroscopy, we also measure throughout a continuous range of n_e in a single experiment and from the same plasma.

Furthermore, we observe our plasma in absorption. This, along with simultaneously observing multiple lines, provides a unique opportunity to experimentally explore occupation probabilities (Hummer & Mihalas 1988) by measuring relative line *strengths*.

In this paper we present spectroscopic measurements of the Hβ line. Historically, theoretical calculations, particularly widths, of this line agree with measurements from benchmark

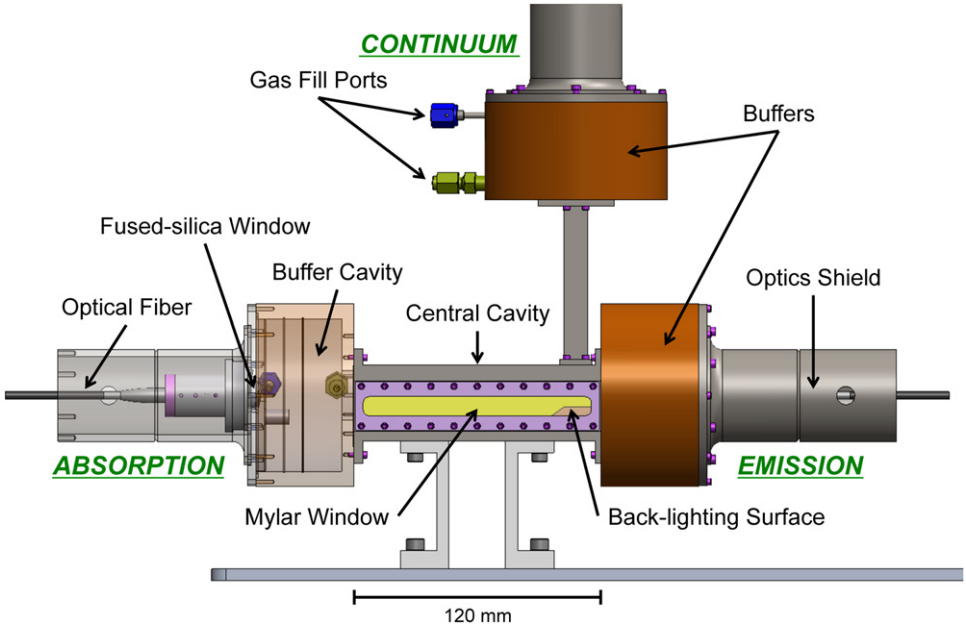

Figure 1. False-color hardware drawing of our "ACE"-configuration gas-cell assembly, capable of simultaneously observing (1) the H plasma in Absorption, (2) the Continuum emission from a gold, back-lighting surface, and (3) the H plasma in emission. For one line of sight we show the hardware within the buffer (orange) and optics shield (gray).

laboratory experiments (e.g., Wiese et al. 1972), validating its accuracy (for $n_e < 10^{17}\,\mathrm{cm}^{-3}$) to diagnose plasma conditions (e.g., Kelleher et al. 1993). We thus fit Hβ to infer electron density, n_e, and $n = 2$ level population, n_2, finding agreement between different theoretical line-profile models (Section 3.3). These n_e and n_2 measurements also allow us to infer electron temperature, T_e (Section 3.4). We then scrutinize our sensitivity to experimental uncertainties. Section 4.1 synthetically investigates the dependence on T_e, and Sections 4.2 and 4.3 investigate inhomogeneities or gradients in the plasma conditions. Our scope is to secure our measured Hβ line as a diagnostic anchor for the investigation of relative line profiles (*shapes* and *strengths*) as part of the laboratory study of WD photospheres.

2. EXPERIMENTAL PLATFORM

Ours is part of the *Z* Astrophysical Plasma Properties (ZAPP) Collaboration (Rochau et al. 2014), a group of experiments conducted simultaneously at the *Z* Pulsed Power Facility (e.g., McDaniel et al. 2002; Matzen et al. 2005; Rose et al. 2010; Savage et al. 2011) at Sandia National Laboratories. ZAPP experiments take place in a large (>60 m^3) vacuum chamber, each making use of the same *z*-pinch dynamic hohlraum (e.g., Spielman et al. 1998; Nash et al. 1999; Stygar et al. 2001; Sanford et al. 2002; Bailey et al. 2006; Rochau et al. 2008) X-ray source to initiate plasma formation.

We place a gas-cell assembly (Figure 1), filled with hydrogen (H_2), a distance away (324 ± 2 mm) from the X-ray source along a radial line of sight (LOS). X-rays irradiate the cell, propagate through a thin ($1.44 \pm 0.02\,\mu$m) Mylar window and through the H_2 gas, and are absorbed by a gold wall at the back end of the cell cavity. The gold heats to an electron temperature of $T_e \sim$ few eV and re-emits as a continuum, which photoionizes the hydrogen.

We observe the H plasma along lines of sight parallel to the gold wall and perpendicular to the photoionizing radiation (Figure 2). For each LOS, a 50-mm-long buffer cavity separates the optics from the plasma formed within the central cavity. Optical fibers deliver the light to time-resolved spectrometer systems. Sections 4.2 and 4.3 elaborate on our observations (Figures 12 and 14 illustrate). See Falcon et al. (2013b) for a description of our experimental platform and plasma formation, and see Falcon et al. (2015) for details of our data processing and calibration.

3. TIME-RESOLVED SPECTROSCOPIC MEASUREMENTS

Inside the gas-cell central cavity a polyhedral stainless steel block, coated with 5 μm of gold, rests on one end. Its surface is tilted with respect to the plane normal to the *z*-pinch X-rays (*y*–*z*) and pitched with respect to the horizontal (*x*–*y*). This allows the X-rays, the optics in one horizontal LOS (absorption), and the optics in the vertical LOS (continuum) to each have a direct view. The X-rays heat this surface like they do the gold back wall, allowing it to serve as a back-light for absorption measurements.

3.1. Extracting Transmission

Absorption spectra of plasmas contain three components:

$$I_\lambda^{\mathrm{meas}} = I_\lambda^{\text{back-light}}\, T_\lambda^{\mathrm{plasma}} + I_\lambda^{\mathrm{plasma}}. \quad (1)$$

$I_\lambda^{\text{back-light}}$ is the spectral radiance of the back-lighting continuum. The transmission, $T_\lambda^{\mathrm{plasma}}$, and the self-emission, $I_\lambda^{\mathrm{plasma}}$, both describe the plasma but in different ways. We focus on $T_\lambda^{\mathrm{plasma}}$ for our analysis because of its preferable signal-to-noise ratio (S/N). It also provides a constraint on relative line strengths because all the transitions of the absorption lines we observe share the same initial (lower) state ($n = 2$); this is a subject of future work.

The components in Equation (1) are separately measurable using the "ACE" gas cell. Because our absorption LOS (I_λ^{abs})

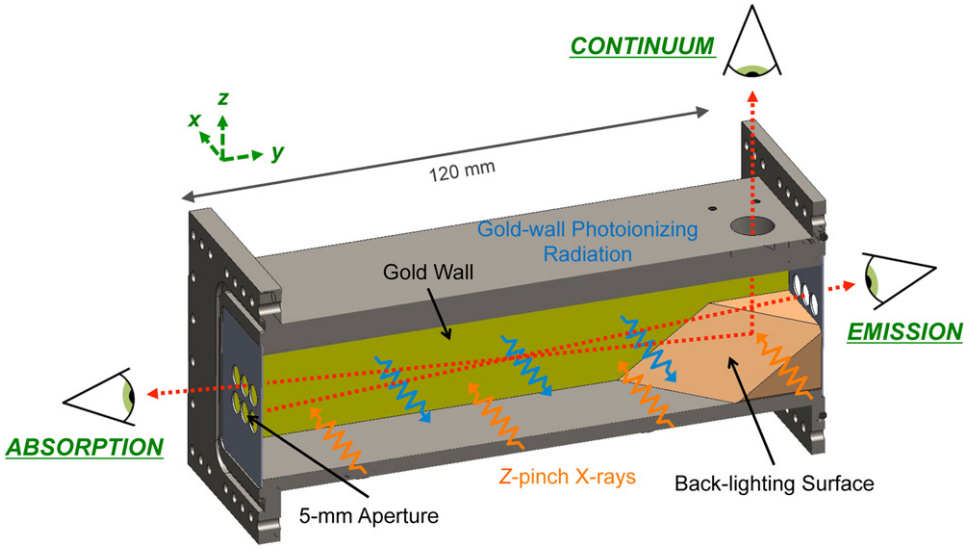

Figure 2. Cross-section false-color hardware drawing of the gas-cell central cavity. We illustrate the three observing lines of light (dashed, red lines). The absorption LOS observes the same area on the back-lighting surface as does the continuum LOS (vertical) but through the length of the plasma-filled cell. The emission LOS also traverses this length but has no back-light. Thus, both horizontal lines of sight observe the same nominal plasma self-emission.

observes a back-lighting surface through a length of plasma, $I_\lambda^{\rm abs}$ equals $I_\lambda^{\rm meas}$. Our continuum LOS, which observes this same back-lighting surface (Figure 2), also measures absorption spectra. However, since the length of intervening plasma is minimal ($L \sim 7$ mm), the transmission is close to unity (absorption is small) and we assume negligible self-emission, so that $I_\lambda^{\rm cont} \approx I_\lambda^{\rm back\text{-}light}$.

With our emission LOS we approximate $I_\lambda^{\rm em}$ to equal $I_\lambda^{\rm plasma}$. The length of plasma this LOS observes ($L \sim 120$ mm) nearly matches that of the absorption LOS ($L \sim 114$ mm), which is ~5% shorter. We also approximate the nature of the plasma emission from each LOS to be the same, though the absorption LOS includes a ~ few-millimeter region adjacent to a gold, back-lighting surface that the emission LOS does not (Figure 2).

Upon placing our measured emission and absorption data onto the same absolute scale (Falcon et al. 2015), we correct the latter for plasma self-emission. We can then substitute our measurements into Equation (1) and invert to extract transmission:

$$T_\lambda^{\rm plasma} \approx \frac{I_\lambda^{\rm abs,cor}}{I_\lambda^{\rm cont}} \approx \frac{I_\lambda^{\rm abs} - I_\lambda^{\rm em}}{I_\lambda^{\rm cont}}. \quad (2)$$

Figure 3 shows an example Hβ corrected-absorption spectrum (solid, red; $I_\lambda^{\rm abs,cor}$) versus its uncorrected spectrum (dotted, red; $I_\lambda^{\rm abs}$) for an integration of the time-resolved data over a 10-ns interval (line-out).

A desirable strategy to address plasma self-emission for absorption data measured for opacity studies is to require a back-lighter that is sufficiently bright to overwhelm self-emission (e.g., Davidson et al. 1988; Perry et al. 1996; Bailey et al. 2007, 2009, 2015). Our simultaneous emission and absorption measurements shed this requirement by allowing us to remove the former from the latter, and since we are the first to study H line profiles in absorption, we are also the first to utilize this technique for H. Consequently, this strategy, and in particular the approximations we list, deserve further scrutiny.

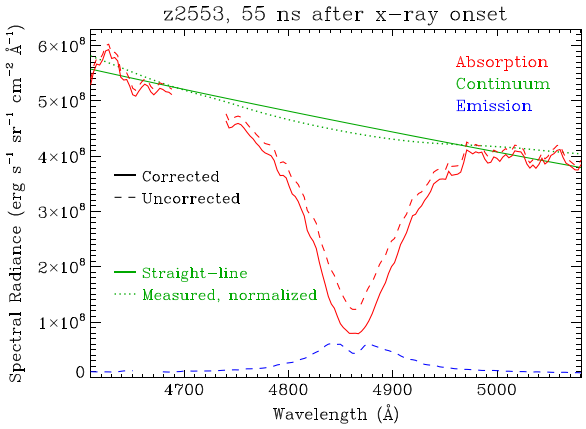

Figure 3. Example Hβ corrected-absorption spectrum (solid, red) plotted with its uncorrected-absorption (dashed, red) and with the subtracted-emission (dashed, blue). These 10-ns line-outs center at 55 ns after the onset of X-rays from experiment z2553. We also show the back-lighting continuum shape measured from z2554 and normalized to the z2553 corrected-absorption. This continuum shape (dotted, green) is similar to the straight-line continuum (solid, green) we use to convert these data to transmission.

At the electron densities we encounter, overlap of the Hβ wings with adjacent lines (i.e., Hα and Hγ) is minimal. Also, we do not observe the bound-free continuum (e.g., Däppen et al. 1987) to reach far enough redward to affect Hβ. To focus on the Hβ bound–bound transition we simplify our transmission extraction by redefining the continuum baseline ($I_\lambda^{\rm cont*}$). Since our measured shapes of the back-lighting continua (using the continuum LOS[3]) are quite linear in the Hβ spectral vicinity (dotted, green in Figure 3), we use straight-line fits (solid,

[3] Because only two spectrometer systems are sufficiently calibrated (Falcon et al. 2015), we do not use the continuum LOS to measure $I_\lambda^{\rm cont}$ ($I_\lambda^{\rm back\text{-}light}$) on experiment z2553. This experiment uses one spectrometer system for the absorption LOS and the second for the emission LOS, enabling the self-emission correction. On the subsequent experiment, z2554, the second spectrometer system uses the continuum LOS to measure the back-lighting spectral shape needed to infer transmission.

green); $I_\lambda^{\rm cont*} \approx I_\lambda^{\rm cont}$. This circumvents potential contamination due to any additional continuous (weakly dependent on wavelength) opacity sources, such as that due to the H^- ion (e.g., Wishart 1979; Griem 1997).

3.2. Spectral-line Fitting Model

Our fitting model is the transmission due to bound–bound absorption of a hydrogen Balmer line for a homogeneous (single T_e, n_e, and n_l) plasma:

$$T_\lambda^{\rm b-b} = \psi * \exp\left\{-\kappa_\lambda^{\rm b-b} L\right\}, \quad (3)$$

where ψ is the measured instrumental broadening, * is the convolution operator, $\kappa_\lambda^{\rm b-b}$ is the opacity due to photoexcitation for a bound–bound transition while neglecting stimulated emission (e.g., Mihalas 1978), and L is the length of the observed plasma.

We express the opacity as

$$\kappa_\lambda^{\rm b-b} = \frac{\pi e^2}{m_e c} f_{l\to u} n_l w_u(n_e) \phi_\lambda(T_e, n_e), \quad (4)$$

where e is the electron charge, m_e is the electron mass, c is the speed of light, $f_{l\to u}$ is the oscillator strength of the transition from the lower to upper energy level, and n_l is the lower-level population. The upper-level occupation probability, $w_u(n_e)$, depends on electron density (Hummer & Mihalas 1988). The line profile, $\phi_\lambda(T_e, n_e)$, is normalized ($\int \phi_\lambda d\lambda = 1$) and a function of both electron temperature, T_e, and n_e. Because the dependence on T_e is relatively weak (Section 4.1) and because we have empirical constraints (Section 3.4), our fits assume $T_e = 1.0$ eV.

Combining the constants into a single factor, C_κ, and specifying the Hβ transition, Equation (3) becomes

$$T_\lambda^{\rm H\beta} = \psi * \exp\left\{-C_\kappa f_{2\to 4} n_2 w_4(n_e) \phi_\lambda^{\rm H\beta}(n_e) L\right\}. \quad (5)$$

The principal quantum numbers of the initial and final states are $n = 2$ and $n = 4$, respectively.

We use oscillator strengths from Baker (2008), who reports to high precision (<0.3% uncertainty). The occupation probability comes from Seaton (1990); for Hβ, $w_u(n_e)$ is quite nearly unity. We fix L according to the dimensions of our gas-cell hardware design. This leaves n_2 and $\phi_\lambda^{\rm H\beta}(n_e)$ to be determined from experiment.

3.3. Fits to Measured Hβ Transmission

Figures 4 and 5 plot 12 consecutive 10-ns line-outs of Hβ transmission (black diamonds) we measure from experiment z2553; the first line-out begins at the onset of X-rays (centered at 5 ns after onset). Uncertainties in spectral points (black, vertical lines) reflect the S/N.

We use a Levenberg–Marquardt minimization (Levenberg 1944; Marquardt 1963) to fit our measured transmission spectra with Equation (5). Red, blue, pink, and green curves correspond to fits using theoretical line profiles, $\phi_\lambda^{\rm H\beta}$, that follow Vidal et al. (1973, VCS), Tremblay & Bergeron (2009, TB), Gigosos et al. (2003, GGC), and T.A. Gomez et al. (2015, in preparation, Xenomorph or XENO), respectively. The VCS profiles come from Lemke (1997).

These theoretical line profiles are quite similar, differing noticeably only in the line center (enlarged window in lower left-hand side of each panel). Fits using VCS and TB—both based on the Unified Theory—are nearly identical. Fits using GGC and Xenomorph—both incorporating computer simulations (e.g., Stamm et al. 1984; Stambulchik & Maron 2010)—exhibit less-pronounced central humps,[4] and this latter theory is the only one of the four that calculates asymmetry.

We indeed measure structure in the line center, including asymmetry (e.g., Kudrin & Sholin 1963; Wiese et al. 1975; Halenka 1988; Djurović et al. 2005). This structure remains absent at the lowest n_e and increases with this parameter. Early and late in the experiment the fits reproduce our measurements near the line center quite well, but from 35 to 95 ns there are statistically significant deviations. The fits predict central structure that we do not observe over this duration of the experiment, which spans the range of $1 \times 10^{17} \lesssim n_e \lesssim 3 \times 10^{17}$ cm^{-3}. Further work is required to ascertain whether this is due to deficiencies in the theoretical line profiles or in the experiment.

GGC and Xenomorph profiles provide systematically better fits, as expressed by reduced $\chi^2_{\rm red}$ (Figure 6). Though the VCS and TB profiles yield poorer fits, all theories infer values for electron density, n_e, and lower ($n = 2$) level population, n_2, that agree (Figures 7 and 8, respectively). The standard deviation of n_e between theories increases from $\lesssim$2 to $\sim$ 6% of $\langle n_e \rangle$ as time increases (as n_e increases). For n_2, the trend is the same, increasing from $\lesssim$2 to $\sim$ 4%.

We monitor n_e increase throughout the first 95 ns of experiment z2553 before reaching a plateau of $n_e \sim 3 \times 10^{17}$ cm^{-3}. Beyond 55 ns we do not plot n_e inferred using GGC profiles, because these values extend beyond the n_e range covered by Gigosos et al. (2003). In the first 25 ns we overlap ($4 \times 10^{16} \lesssim n_e \lesssim 10^{17}$ cm^{-3}) the electron-density range observed by Wiese et al. (1972)—the only other study to measure multiple H Balmer lines near these conditions. We then exceed it by approximately a factor of 3.

The right-hand side, vertical axis of Figure 7 shows the ionization, which we define as $\frac{n_e}{n_e + n^0}$, where n^0 is the neutral H atom density. To determine the total particle density ($n_{\rm tot} = n_e + n^0$), we measure the initial H_2-gas fill pressure inside our cell in situ using piezoresistive pressure sensors (see Appendix A in Falcon 2014). Assuming that the photoionizing radiation forming our plasma completely dissociates the H_2, the Ideal Gas Law translates our measured pressure ($P = 10.63 \pm 0.05$ Torr) to $n_{\rm tot} = (6.92 \pm 0.08) \times 10^{17}$ cm^{-3}. Uncertainties for P and $n_{\rm tot}$ reflect the precision of the pressure-sensor voltage measurement. They do not include all systematic uncertainties, such as that due to the accuracy of the correction for zero-pressure output voltage.

3.4. Electron-temperature Determination

The lower-level population (n_2) also increases with time after exhibiting a moderate spike soon (~20 ns) after the onset of X-rays (Figure 8). To give our measured n_2 context, we compare it to that of a plasma in local thermodynamic equilibrium (LTE) by plotting the ratio (open diamonds connected by dotted lines and corresponding to the purple,

[4] The central feature of a line profile is usually described as the central *dip* because it is usually observed in emission. In our novel approach, however, we observe the profile in absorption.

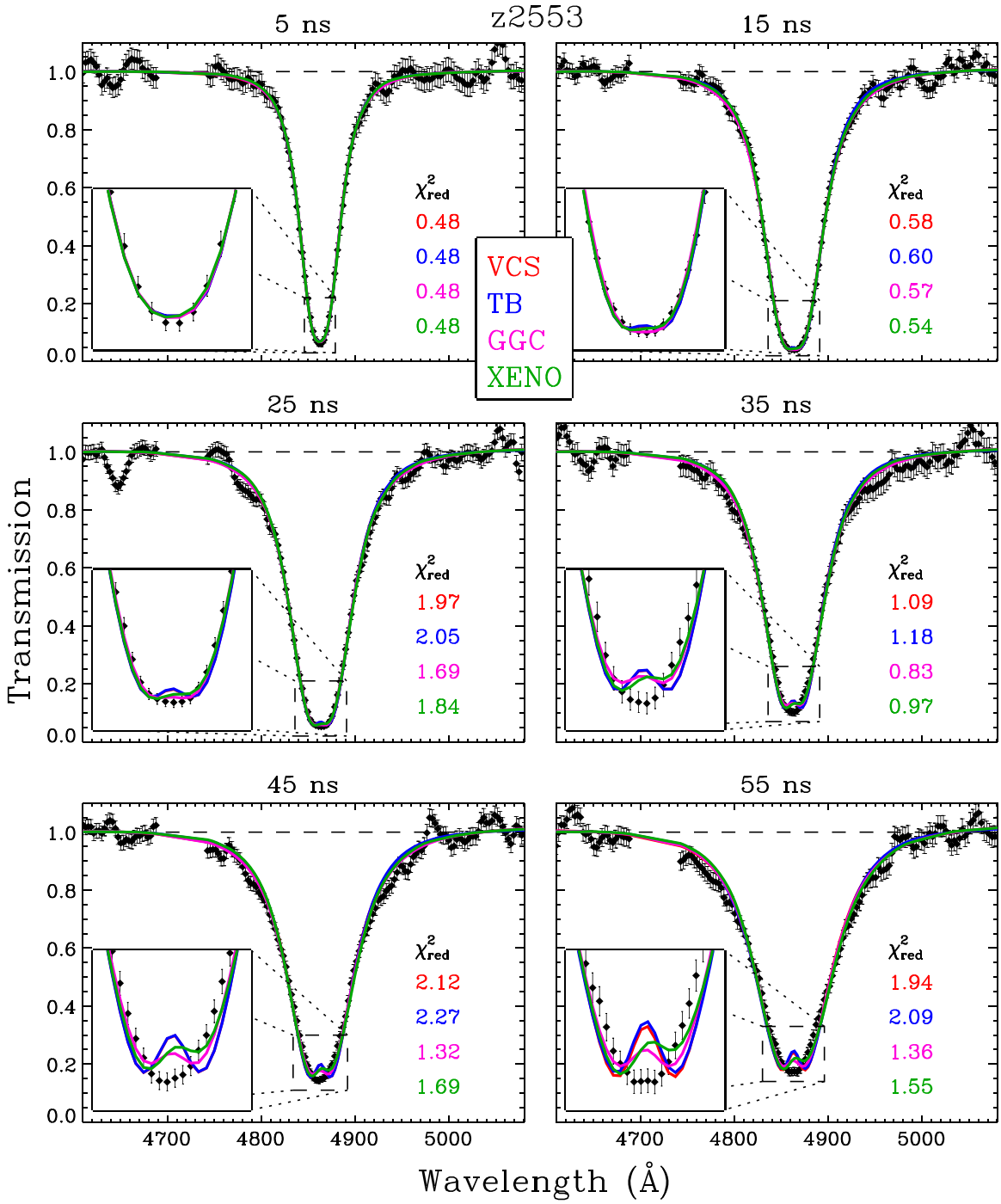

Figure 4. Time sequence of Hβ transmission spectra (black diamonds) measured from our laboratory plasma during experiment z2553. Uncertainties (black, vertical lines) reflect the signal-to-noise ratio. The first of these 10-ns line-outs begins at the onset of X-rays to the gas cell. Fits (solid curves) use the theoretical line profiles of Vidal et al. (1973, VCS; red), Tremblay & Bergeron (2009, TB; blue), Gigosos et al. (2003, GGC; pink), and T.A. Gomez et al. (2015, in preparation, XENO; green). We look closely at the line center where the fits differ most.

right-hand axis). We determine the LTE $n = 2$ population by first inserting our inferred electron density and measured total particle density into the Saha equation and solving for electron temperature. We neglect ionization potential depression (e.g., Crowley 2014) and approximate all neutral atoms to be in the ground state ($n^0 \approx n_1$):

$$\frac{n_e^2}{n_{tot} - n_e} \approx \frac{n_e^2}{n_1} \approx \left(\frac{2\pi m_e k T_e}{h^2}\right)^{3/2} \exp\left\{\frac{-\epsilon^0}{kT_e}\right\}, \quad (6)$$

where k is the Boltzmann constant, h is the Planck constant, and the neutral-hydrogen ionization energy is $\epsilon^0 = 13.6$ eV.

Then, using this T_e with the Boltzmann relation yields n_2(LTE):

$$\frac{n_2(\mathrm{LTE})}{n_1} = \frac{g_2}{g_1} \exp\left\{\frac{-(\epsilon_2 - \epsilon_1)}{kT_e}\right\}, \quad (7)$$

where the statistical weight, g_n, equals $2n^2$, and the energy difference between the $n = 2$ and $n = 1$ states is $\epsilon_2 - \epsilon_1 = 10.2$

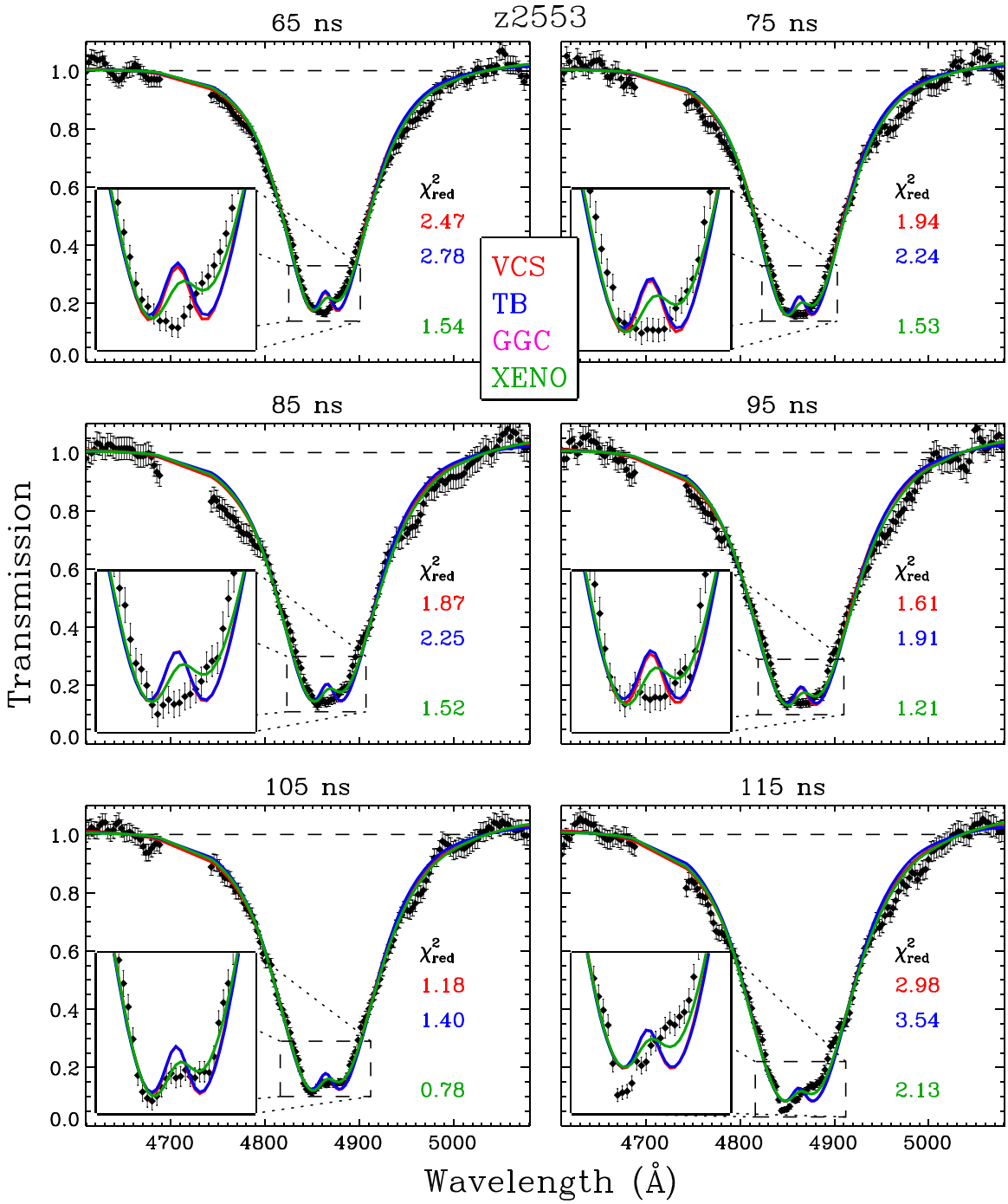

Figure 5. Same as Figure 4 but plotting the subsequent six 10-ns line-outs. Here we do not include GGC fits since the inferred electron densities exceed the range spanned by the GGC line-profile grid.

eV. Early in time, our measured n_2 is ~5 times that at LTE (dashed, purple, horizontal line). This ratio $(\frac{n_2(\text{measured})}{n_2(\text{LTE})})$ monotonically approaches unity and reaches it ~55 ns after the onset of X-rays. This implies that the ionization fraction, $n = 2$ population, and $n = 1$ population are consistent with their LTE values.

Once in LTE, $T_e \sim 1.25$ eV (~14,500 K) and rises to T_e ~1.35 eV (~15,700 K) by ~115 ns (Figure 9). Before ~55 ns, our LTE T_e estimate provides an upper limit (open diamonds, dotted lines) to the true T_e, assuming our plasma is "overionized" (e.g., Kawasaki et al. 2002). Our measurement of "overexcitation" (i.e., elevated $n = 2$ population) supports this assumption, as does the premise that our plasma is initially photoionized (Falcon et al. 2013b).

3.5. Uncertainties in Inferred Plasma Conditions

The uncertainties for our inferred n_e (Figure 7), n_2 (Figure 8), and, subsequently, T_e (Figure 9) have two sources, which we add in quadrature. σ^{fit} is from the fit, which is a random uncertainty due to noise in the spectra. It is typically ~2% and ~1% for n_e and n_2, respectively. σ^{cal} is due to the transmission

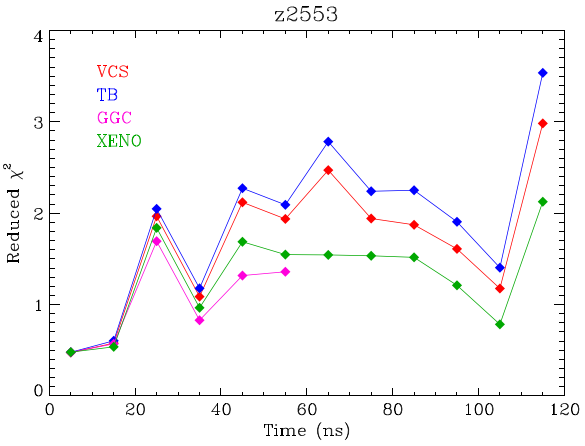

Figure 6. Goodness-of-fit (reduced chi squared, $\chi^2_{\rm red}$) vs. time for fits to Hβ transmission measured from experiment z2553 and using VCS (red), TB (blue), GGC (pink), and Xenomorph (green) line profiles. Early in time when n_e is low, all theories provide equally good fits. Later in time when $n_e \gtrsim 10^{17}$ cm^{-3}, GGC and Xenomorph profiles provide better fits than VCS and TB.

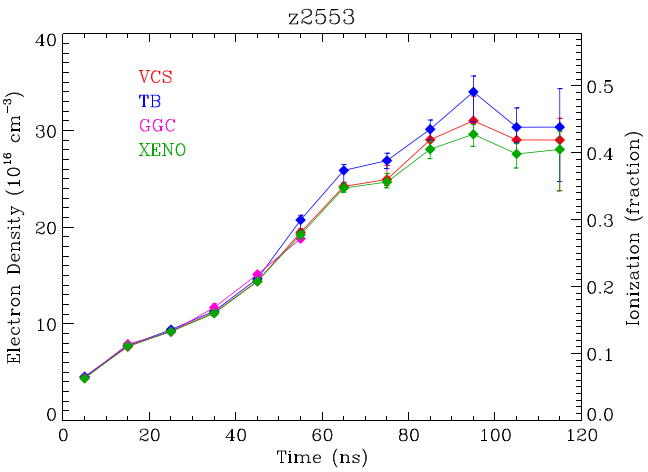

Figure 7. Electron density (left-hand side, vertical axis) and ionization (right-hand side, vertical axis) vs. time determined from fits to measured Hβ transmission. Section 3.5 describes uncertainties (vertical lines). We time-resolve a smooth increase in electron density (n_e) which allows us to measure line profiles throughout a range of n_e in a single experiment and from the same plasma. All theories infer n_e in agreement.

extraction (Section 3.1), which depends upon the accuracy of our calibration (i.e., the relative measurement of plasma emission and absorption from different spectrometer systems; Falcon et al. 2015).

Early in time, the magnitude of $\sigma^{\rm cal}$ is similar to that of $\sigma^{\rm fit}$. Throughout the experiment, however, $\sigma^{\rm cal}$ increases to $\sim$ several %. This is a result of the evolution of the back-lighting continuum emission ($I_\lambda^{\rm cont}$) which decreases as the gold surface cools, thus increasing the significance of the self-emission component ($I_\lambda^{\rm em}$) to the measured absorption ($I_\lambda^{\rm abs}$).

3.6. Plasma Reproducibility

We observe the same qualitative trends in goodness-of-fit, electron density (Figure 10), and lower-level population versus time across multiple experiments, giving credence to plasma reproducibility using our experimental platform. This includes the n_2 spike at ~20 ns.

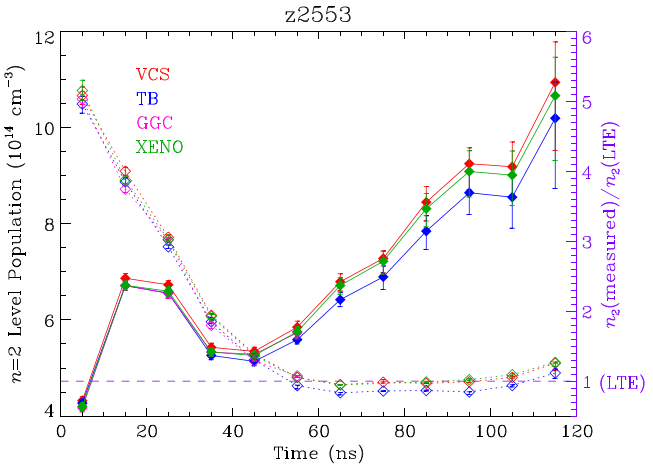

Figure 8. Left-hand side axis: similar to Figure 7 but for lower ($n = 2$) level population vs. time. Right-hand side axis: ratio of measured vs. LTE $n = 2$ population (open diamonds, dotted lines). By ~ 55 ns after the onset of X-rays the $n = 2$ population is at its LTE value (dashed, purple, horizontal line).

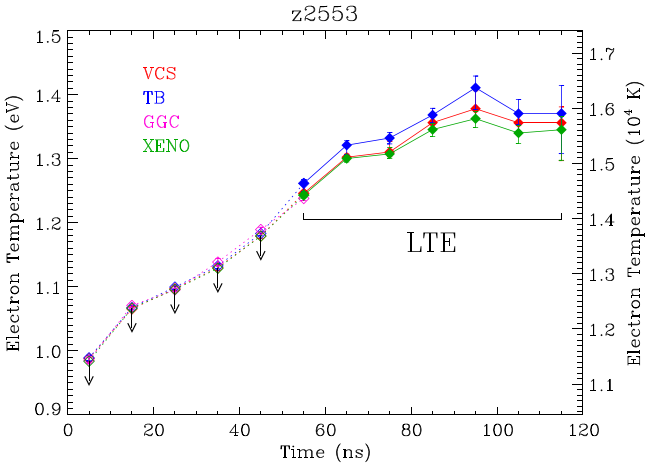

Figure 9. Electron temperature (T_e) vs. time inferred from the Saha equation assuming local thermodynamic equilibrium (LTE) and using our measured ionization fraction (diamonds). Before the plasma reaches LTE at ~55 ns (Figure 8), these inferred T_e values are upper limits assuming the plasma is "overionized" (see the text).

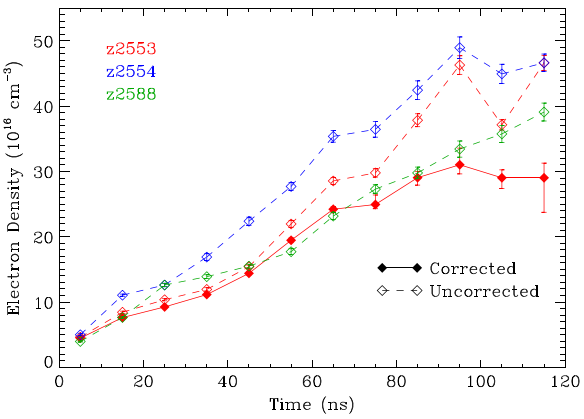

Figure 10. Similar to Figure 7. The inferred electron density vs. time from multiple experiments is qualitatively reproducible. Also, fits to Hβ transmission uncorrected (open diamonds, dashed lines) for plasma self-emission overestimate the electron density compared to fits with the correction (filled diamonds, solid lines). We show fits using VCS theoretical line profiles.

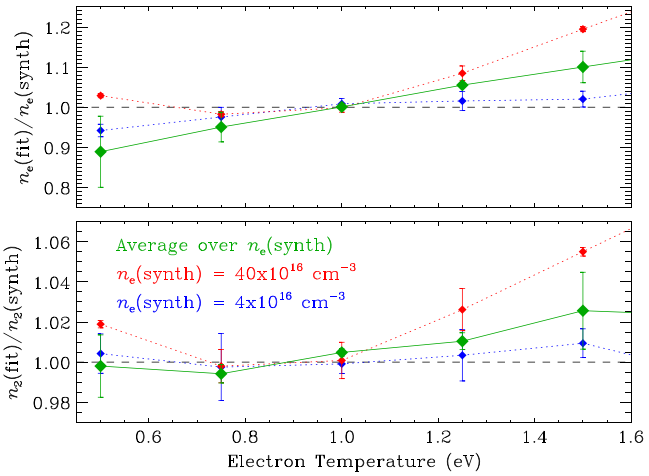

Figure 11. Ratio (vertical axis) of inferred parameter (fit) and the value of that parameter for synthetic Hβ transmission (synth) created at different electron temperatures (horizontal axis). Our fits assume $T_e = 1.0$ eV. Top and bottom panels show inferred electron density, n_e, and lower ($n = 2$) level population, n_2, respectively.

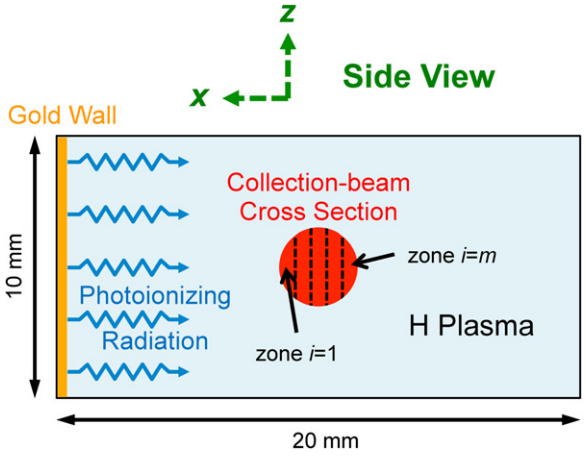

Figure 12. Cross-section schematic of the gas-cell central cavity from the point of view of a horizontal line of sight. The collection beam (red) traverses the hydrogen plasma parallel to the gold wall and perpendicular to the photoionizing radiation. We construct synthetic data simulating a transverse gradient in electron density, n_e, by assembling the collection beam out of zones with different n_e linearly decreasing with distance from the gold wall (x direction).

Experiments z2554 (blue) and z2588 (green) have no I_λ^{em} measurement, so we infer n_e from fits to I_λ^{abs} (i.e., transmission uncorrected for plasma self-emission; open diamonds, dashed lines). For z2553 (red), foregoing the emission correction overestimates n_e by ~few% early in time, increasing to ~few tens of % late in time. It also underestimates n_2 by percentages similar to the n_e overestimations.

4. SYNTHETIC INVESTIGATIONS INTO SYSTEMATIC UNCERTAINTIES

Our fitting procedure (Section 3.2) approximates the line profile, $\phi_\lambda^{H\beta}$, to have a negligible dependence on electron temperature, T_e, and therefore depend solely on electron density, n_e. It also assumes that our experimental plasma either (1) is homogeneous and exists at a single plasma condition or (2) can be sufficiently and uniquely described as a homogeneous plasma.

We implement synthetic data analysis (e.g., Nagayama et al. 2012a, 2012b) to investigate the sensitivity of our fits to the aforementioned factors. We simulate Hβ transmission data at different T_e (Section 4.1) as well as those resulting from inhomogeneous conditions (Sections 4.2 and 4.3). These data use VCS theoretical line profiles, and include random noise (S/N = 33) and instrumental broadening (Voigt profile with ~10-Å FWHM) typical for our experiments. They also span a range of plasma conditions (i.e., $10^{16} \leqslant n_e \leqslant 4 \times 10^{17}$ cm^{-3} in steps of $\Delta n_e = 3 \times 10^{16}$ cm^{-3} and $3 \times 10^{14} \leqslant n_2 \leqslant 1.2 \times 10^{15}$ cm^{-3} in steps of $\Delta n_2 = 10^{14}$ or 3×10^{14} cm^{-3}). We independently adjust T_e, n_e, and n_2 without assuming LTE.

4.1. Sensitivity to Electron Temperature

Our ionization fraction ($\frac{n_e}{n_{tot}}$) and n_2 measurements indicate that our plasma reaches LTE by ~55 ns (Figure 8). This corresponds to a thermalized temperature of T_e ~1.3 eV (~15,000 K). Before this time and while our plasma is not in LTE, we assume that our T_e estimates are upper limits (Figure 9); a precise T_e determination is nontrivial, likely requires collisional-radiative hydrodynamic modeling (e.g., Hansen et al. 2007), and is beyond the scope of this paper. Because of this and because of the relative insensitivity we show in Figure 11, we adopt a compromise (as a function of time and hence T_e) by fixing $T_e = 1.0$ eV in our spectral-line fitting model (Section 3.2).

By assuming $T_e = 1.0$ eV, our fits underestimate n_e (top panel) and n_2 (bottom panel) for cooler ($T_e < 1.0$ eV) plasmas and overestimate for warmer ($T_e > 1.0$ eV) plasmas. This effect is more significant for n_e than for n_2, for which it is quite small ($\lesssim$1% for most cases). Uncertainties (vertical lines) only simulate σ^{fit} and do not include σ^{cal} (Section 3.5).

4.2. Gradient in Electron Density Transverse to Our Line of Sight

As a consequence of the plasma formation inside our gas cell, ionization decreases with increasing distance from the gold wall (Falcon et al. 2013b). Since we observe our plasma parallel to the gold wall (perpendicular to the photoionizing radiation) along lines of sight with finite diameter (~3 mm; Falcon et al. 2015), our measured spectra sample some range of plasma conditions.

We simulate a linear gradient in n_e transverse (x direction) to our LOS using the mean of synthetic homogeneous transmission spectra of different n_e weighted according to fractional areas of a circle. This corresponds to our cylindrical collection beam. We describe the gradient as the difference of n_e at the boundaries of the LOS collection beam divided by the mean n_e:

$$\text{Gradient} \equiv \frac{|n_e(i=m) - n_e(i=1)|}{\frac{1}{m}\sum_{i=1}^{m} n_e(i)} \times 100\%, \qquad (8)$$

where zone i is one of m zones (Figure 12).

The top and bottom panels of Figure 13 plot our results for n_e and n_2, respectively. We show the ratio (colored diamonds) of the parameter inferred from fitting and the synthetic value the fit sought to recover (i.e., $\frac{n_e(\text{fit})}{n_e(\text{synth})}$ and $\frac{n_2(\text{fit})}{n_2(\text{synth})}$). For n_e, this synthetic value is the mean n_e across zones, and, since the gradient is linear, it equals that of the central zone.

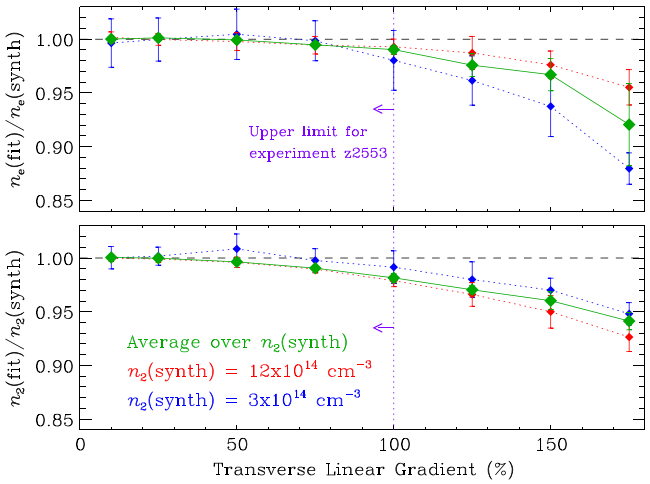

Figure 13. Vertical axis: ratio of inferred parameter (fit) and the value of that parameter used to create synthetic Hβ transmission (synth) that simulates a linear gradient in electron density, n_e, transverse (x direction) to the observed line of sight (LOS). Horizontal axis: n_e gradient transverse to synthetic LOS defined in Equation (8). Top and bottom panels show inferred n_e and lower ($n = 2$) level population, n_2, respectively. The steeper the gradient, the more the fit underestimates each parameter.

As the gradient increases, fits underestimate both n_e and n_2. Empirically, we find that neither $\frac{n_e(\text{fit})}{n_e(\text{synth})}$ nor $\frac{n_2(\text{fit})}{n_2(\text{synth})}$ depend on n_e, so we average over this parameter. They do depend on n_2, however. As n_2 (line strength) increases, fits underestimate n_e less and n_2 more.

Though an exponential function better describes the decrease in measured n_e with increasing distance from the gold wall (Falcon et al. 2013b), we approximate this gradient to be linear across our 3-mm diameter collection beam. The measured gradient from experiments z2300 and z2302 is then ~100% for a LOS centered at 10 mm away from the gold wall and using a ~30 Torr H_2 gas fill (Falcon et al. 2013b). Our synthetic test suggests that this could lead to an underestimate of both n_e and n_2 of up to ~3%.

Experiment z2553 uses a ~10-Torr gas fill. Lower pressure results in decreased attenuation of the photoionizing radiation with increasing distance from the gold wall. This means we encounter higher n_e for a fixed LOS distance. It also means the transverse gradient is not as steep. Therefore, the measured ~100% gradient should be an overestimate for the z2553 observing LOS (dotted, purple, vertical line). The underestimation of n_e and n_2 is then $\lesssim$3%.

4.3. Gradient in Electron Density along Our Line of Sight or a Boundary-layer Plasma

An inevitable attribute of laboratory plasmas is their finite size. Boundary layers exist where conditions transition away from that of the bulk plasma, contributing to inhomogeneity along the LOS. Observing long plasmas minimizes this effect (e.g., Bengtson & Chester 1976), and though we create the longest photoionized (radiation-driven) laboratory plasmas to date (Falcon et al. 2013b), their lengths remain finite.

We assume that the boundary-layer plasma extending into the buffer cavity (Figure 1) is the dominant source of inhomogeneity along our observing LOS (y direction). Thus, we create synthetic data consisting of two components: a homogeneous plasma (solid, red in Figure 14) the length (L ~114 mm) of the absorption LOS inside our gas-cell central cavity, and a boundary layer (diagonally striped, red) with variable length whose n_e linearly decreases along that length toward the observer. This homogeneous component neglects the region adjacent to the gold, back-lighting surface (Section 3.1), and the boundary-layer n_e does not decrease to zero from the electron density, n_e(synth), of the homogeneous component. It decreases to the lowest value of our theoretical line-profile grid, $n_e = 10^{15}$ cm^{-3}.

A synthetic boundary layer in the foreground of a homogeneous plasma causes fits to underestimate n_e and overestimate n_2 (Figure 15). Longer boundary layers exacerbate these effects. Empirically, they do not depend on n_2 (similarly to the lack of n_e-dependence of $\frac{n_e(\text{fit})}{n_e(\text{synth})}$ and $\frac{n_2(\text{fit})}{n_2(\text{synth})}$ for the transverse gradient in Section 4.2), so we average over this parameter. As n_e(synth) increases, fits underestimate n_e more and overestimate n_2 less.

With current measurements, the true conditions in the buffer cavity are difficult to ascertain. As a conservative estimate, though, we do not expect a boundary-layer plasma to extend beyond ~15 mm (dotted, purple, vertical line) into the 50-mm-long buffer. In similar experiments we measure n_e to significantly fall off at 15 mm from the gold wall (Falcon et al. 2013b). This is in the x direction, perpendicular to the gold wall, where the LOS to the photoionizing radiation is direct, thus maximizing the irradiance. Not only is the LOS to a boundary layer peripheral, a 5-mm diameter aperture partitions the central cavity from the buffer cavity (Figures 2 and 14), choking the radiation that can penetrate. At 15 mm our synthetic test suggests that we underestimate n_e and overestimate n_2 by $\lesssim$14%.

5. CONCLUSIONS

We examine hydrogen Balmer-β spectral line profiles measured from laboratory plasmas at WD photospheric conditions; we establish this line as a diagnostic anchor for our experiments. This sets the stage for the analysis of the relative line shapes and strengths of multiple H Balmer lines we measure simultaneously (Hβ, Hγ, and Hδ).

The conditions we encounter during a single experiment smoothly increase throughout a 120-ns plasma evolution and span from n_e ~4 to ~30×10^{16} cm^{-3}, exceeding, by a factor of three, the highest n_e achieved in the benchmark work of Wiese et al. (1972). At $n_e \gtrsim 10^{17}$ cm^{-3}, we find that the theoretical line profiles adopted throughout the WD astronomy community (i.e., Lemke 1997; Tremblay & Bergeron 2009) do not fit our measured Hβ profiles as well as computer-simulation-based calculations (i.e., Gigosos et al. 2003; T.A. Gomez et al. 2015, in preparation). Despite this, all these profiles infer similar n_e and $n = 2$ level populations, n_2; the standard deviations of inferred parameters between theories remain modest, increasing, as n_e increases, from $\lesssim$2 to ~6% of $\langle n_e \rangle$ and from $\lesssim$2 to ~4% of $\langle n_2 \rangle$.

We investigate the sensitivity of our spectral-line fitting model to the following factors: (1) the approximation that the Hβ line shape has a negligible dependence on electron temperature, (2) a gradient in n_e transverse to our observing LOS, and (3) an interloping boundary-layer plasma along our LOS.

For each of these we have experimental guidance. (1) By monitoring n_2 we witness our photoionized plasma smoothly relax into LTE in ~55 ns, which corresponds to $T_e \sim 1.3$ eV

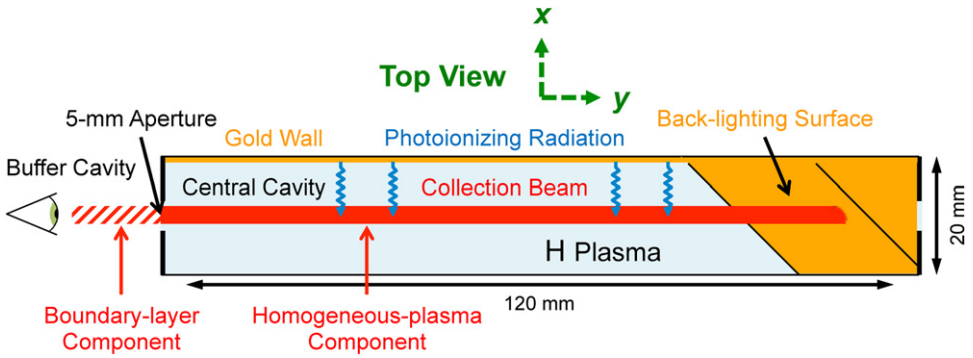

Figure 14. Top-view cross-section schematic of the gas-cell central cavity. We construct synthetic data simulating a line-of-sight gradient in electron density by appending a foreground boundary layer (diagonally striped, red) to the homogeneous-plasma component (solid, red) within a collection-beam volume.

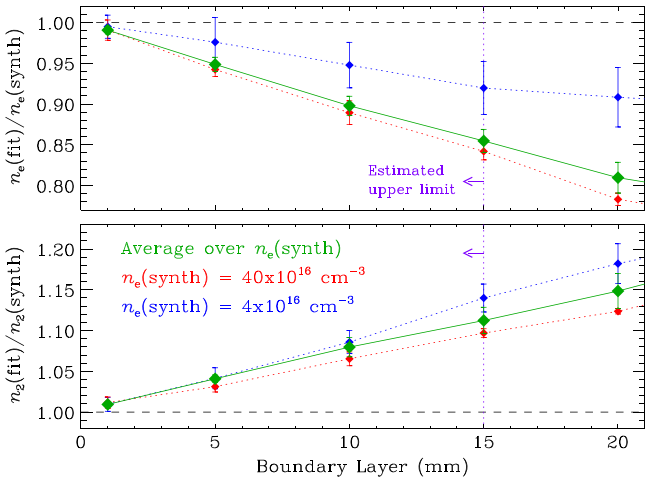

Figure 15. Vertical axis: ratio of inferred parameter (fit) and the value of that parameter used to create synthetic Hβ transmission (synth) that simulates a boundary-layer plasma in the foreground of a homogeneous plasma. Horizontal axis: length of synthetic boundary layer. The longer this layer, the more each fit underestimates n_e (top panel) and overestimates n_2 (bottom panel).

(~15,000 K). Since our fits assume $T_e = 1.0$ eV, we may overestimate n_e by $\lesssim$10% (at our highest n_e) and n_2 by $\lesssim$3%. (2) and (3) Using this experimental platform, we measure n_e of a similar H plasma along LOS at different distances from the radiating gold wall (Falcon et al. 2013b). This constrains the transverse gradient across our LOS for this experiment to be $\lesssim$100%. It also suggests that a boundary-layer plasma along our LOS is, conservatively, $\lesssim$10% of our homogeneous-plasma length. Due to (2), we should underestimate both n_e and n_2 by $\lesssim$3%. Due to (3) we should underestimate n_e and overestimate n_2 by $\lesssim$14%.

Our ability to measure multiple H lines simultaneously at high electron densities ($n_e > 10^{17}$ cm^{-3}) provides us with a sensitive and unprecedented test of theoretical line profiles. Relative H Balmer line *shapes* can discriminate between theories (e.g., Vidal et al. 1973; Tremblay & Bergeron 2009); because we measure in *absorption*, relative line *strengths* will offer a new perspective on occupation probabilities (Hummer & Mihalas 1988).

This work was performed at Sandia National Laboratories and is supported by the Laboratory Directed Research and Development program. We thank the *Z* Facility teams and in particular, D. Bliss, A. Carlson, T. Lockard, L. Nielsen-Weber, and D. Sandoval, for experimental support. Sandia is a multiprogram laboratory operated by Sandia Corporation, a Lockheed Martin Company, for the United States Department of Energy under contract DE-AC04-94AL85000. We thank P.-E. Tremblay for providing TB theoretical line profiles. We also thank R. Bengtson, S. Hansen, and G. Loisel for useful discussions and A. Wootton for championing our fundamental-science research effort. R.E.F., M.H.M., and D.E.W. acknowledge support from the United States Department of Energy under grant DE-SC0010623. T.A.G acknowledges support from the National Science Foundation Graduate Research Fellowship under grant DGE-1110007. This work has made use of NASA's Astrophysics Data System Bibliographic Services.

REFERENCES

Bailey, J. E., Chandler, G. A., Mancini, R. C., et al. 2006, PhPl, 13, 056301
Bailey, J. E., Nagayama, T., Loisel, G. P., et al. 2015, Natur, 517, 56
Bailey, J. E., Rochau, G. A., Iglesias, C. A., et al. 2007, PhRvL, 99, 265002
Bailey, J. E., Rochau, G. A., Mancini, R. C., et al. 2009, PhPl, 16, 058101
Baker, J. 2008, Transition Probabilities for One Electron Atoms, Technical Note 1612 (Washington, DC: Natl. Inst. Stand. Technol.)
Bengtson, R. D., & Chester, G. R. 1976, PhRvA, 13, 1762
Bengtson, R. D., Miller, M. H., Davis, W. D., & Greig, J. R. 1969, ApJ, 157, 957
Crowley, B. J. B. 2014, HEDP, 13, 84
Däppen, W., Anderson, L., & Mihalas, D. 1987, ApJ, 319, 195
Davidson, S. J., Foster, J. M., Smith, C. C., et al. 1988, ApPhL, 52, 847
Djurović, S., Ćirišan, M., Demura, A. V., et al. 2009, PhRvE, 79, 046402
Djurović, S., Nikolić, D., Savić, I., et al. 2005, PhRvE, 71, 036407
Falcon, R. E. 2014, PhD thesis, Univ. Texas, TX, Austin
Falcon, R. E., Bliss, D. E., Carlson, A. L., et al. 2015, Sandia National Laboratories Report, No. SAND2015-3955
Falcon, R. E., Rochau, G. A., Bailey, J. E., et al. 2013a, in ASP Conf. Ser. 469, 18th European White Dwarf Workshop, ed. J. Krzesiński et al. (ASP: San Francisco, CA), 405
Falcon, R. E., Rochau, G. A., Bailey, J. E., et al. 2013b, HEDP, 9, 82
Falcon, R. E., Rochau, G. A., Bailey, J. E., et al. 2010b, in AIP Conf. Proc. 1273, 17th European White Dwarf Workshop, ed. K. Werner & T. Rauch (AIP: Melville, NY), 436
Falcon, R. E., Winget, D. E., Montgomery, M. H., & Williams, K. A. 2010a, ApJ, 712, 585
Gigosos, M. A., González, M. Á, & Cardeñoso, V. 2003, AcSpe, 58, 1489
Griem, H. R. 1997, Principles of Plasma Spectroscopy (Cambridge: Cambridge Univ. Press)
Halenka, J. 1988, JQRST, 39, 347
Hansen, S. B., Bauche, J., Bauche-Arnoult, C., & Gu, M. F. 2007, HEDP, 3, 109
Helbig, V., & Nick, K. 1981, JPhB, 14, 3573
Hill, R. A., & Gerardo, J. B. 1967, PhRv, 162, 45
Hummer, D. G., & Mihalas, D. 1988, ApJ, 331, 794
Kawasaki, M. T., Ozaki, M., Nagase, F., et al. 2002, ApJ, 572, 897
Kelleher, D. E., Wiese, W. L., Helbig, V., et al. 1993, PhST, 47, 75
Kleinman, S. J., Kepler, S. O., Koester, D., et al. 2013, ApJS, 204, 5

Kudrin, L. P., & Sholin, G. V. 1963, SPhD, 7, 1015
Lemke, M. 1997, A&AS, 122, 285
Levenberg, K. 1944, QApMa, 2, 164
Liebert, J., Bergeron, P., & Holberg, J. B. 2005, ApJS, 156, 47
Liedahl, D. A. 2011, Ap&SS, 336, 251
Limoges, M., & Bergeron, P. 2010, ApJ, 714, 1037
Mancini, R. C., Bailey, J. E., Hawley, J. F., et al. 2009, PhPl, 16, 041001
Marquardt, D. W. 1963, J. Soc. Indust. Appl. Math., 11, 431
Matzen, M. K., Sweeney, M. A., Adams, R. G., et al. 2005, PhPl, 12, 055503
McDaniel, D. H., Mazarakis, M. G., Bliss, D. E., et al. 2002, in AIP Conf. Proc. 651, 5th Int. Conf. on Dense Z-Pinches, ed. J. Davis, C. Deeney & N. R. Pereira (AIP: Melville, NY), 23
Mihalas, D. 1978, Stellar Atmospheres (2nd ed.; San Francisco, CA: Freeman)
Montgomery, M. H., Falcon, R. E., Rochau, G. A., et al. 2015, HEDP, in press
Morris, J. C., & Krey, R. U. 1968, PhRvL, 21, 1043
Nagayama, T., Bailey, J. E., Rochau, G. A., et al. 2012b, RScI, 83, 100000
Nagayama, T., Mancini, R. C., Florido, R., et al. 2012a, PhPl, 19, 082705
Napiwotzki, R., Christlieb, N., Drechsel, H., et al. 2001, AN, 322, 411
Nash, T. J., Derzon, M. S., Chandler, G. A., et al. 1999, PhPl, 6, 2023
Parigger, C. G., Dackman, M., & Hornkohl, J. O. 2008, ApOpt, 47, G1
Parigger, C. G., Plemmons, D. H., & Oks, E. 2003, ApOpt, 42, 5992
Perry, T. S., Springer, P. T., Fields, D. F., et al. 1996, PhRvE, 54, 5617
Rochau, G. A., Bailey, J. E., Falcon, R. E., et al. 2014, PhPl, 21, 056308
Rochau, G. A., Bailey, J. E., Maron, Y., et al. 2008, PhRvL, 100, 125004
Rose, D. V., Welch, D. R., Madrid, E. A., et al. 2010, PhRvS, 13, 010402
Sanford, T. W. L., Lemke, R. W., Mock, R. C., et al. 2002, PhPl, 9, 3573
Savage, M. E., LeChien, K. R., Lopez, M. R., et al. 2011, in 18th IEEE Pulsed Power Conf. (PPC) (Columbia, MO: Univ. of Missouri), 983
Seaton, M. J. 1990, JPhB, 23, 3255
Smith, E. W., Cooper, J., & Vidal, C. R. 1969, PhRv, 185, 140
Spielman, R. B., Deeney, C., Chandler, G. A., et al. 1998, PhPl, 5, 2105
Stambulchik, E., & Maron, Y. 2010, HEDP, 6, 9
Stamm, R., Smith, E. W., & Talin, B. 1984, PhRvA, 30, 2039
Stygar, W. A., Olson, R. E., Spielman, R. B., & Leeper, R. J. 2001, PhRvE, 64, 026410
Tremblay, P.-E., & Bergeron, P. 2009, ApJ, 696, 1755
Tremblay, P.-E., Bergeron, P., & Gianninas, A. 2011, ApJ, 730, 128
Vidal, C. R., Cooper, J., & Smith, E. W. 1970, JQSRT, 10, 1011
Vidal, C. R., Cooper, J., & Smith, E. W. 1971, JQSRT, 11, 263
Vidal, C. R., Cooper, J., & Smith, E. W. 1973, ApJS, 25, 37
Wiese, W. L., Kelleher, D. E., & Helbig, V. 1975, PhRvA, 11, 1854
Wiese, W. L., Kelleher, D. E., & Paquette, D. R. 1972, PhRvA, 6, 1132
Wiese, W. L., Paquette, D. R., & Solarski, J. E. 1963, PhRv, 129, 1225
Wishart, A. W. 1979, JPhB, 12, 3511